GEOPHYSICS, VOL. 69, NO. 2 (MARCH-APRIL 2004); P. 522–532, 16 FIGS., 1 TABLE.
10.1190/1.1707072

Seismic low-frequency effects in monitoring fluid-saturated reservoirs

Valeri A. Korneev*, Gennady M. Goloshubin‡, Thomas M. Daley*, and Dmitry B. Silin*

ABSTRACT

There is a complex relationship between seismic attributes, including the frequency dependence of reflections and fluid saturation in a reservoir. Observations in both laboratory and field data indicate that reflections from a fluid-saturated layer have an increased amplitude and delayed traveltime at low frequencies, when compared with reflections from a gas-saturated layer. Comparison of laboratory-modeling results with a diffusive-viscous-theory model show that low (<5) values of the quality factor Q can explain the observations of frequency dependence. At the field scale, conventional processing of time-lapse VSP data found minimal changes in seismic response of a gas-storage reservoir when the reservoir fluid changed from gas to water. Low-frequency analysis found significant seismic-reflection-attribute variation in the range of 15–50 Hz. The field observations agree with effects seen in laboratory data and predicted by the diffusive-viscous theory. One explanation is that very low values of Q are the result of internal diffusive losses caused by fluid flow. This explanation needs further theoretical investigation. The frequency-dependent amplitude and phase-reflection properties presented in this paper can be used for detecting and monitoring fluid-saturated layers.

INTRODUCTION

The relationship between seismic response and fluid saturation in a reservoir depends on many factors, such as porosity and permeability of the reservoir rocks, viscosity and compressibility of the fluid, reservoir thickness, and physical properties of the surrounding medium (Johnston and Toksoz, 1981). However, there is a general connection between the character of porous-layer saturation and the seismic response. In particular, when comparing cases of water and gas saturation, Goloshubin et al. (1996) and Goloshubin and Bakulin (1998) observed phase shifts and energy redistribution between different frequencies. Numerical modeling using Biot theory (Goloshubin and Bakulin, 1998) did not explain the observed results. Recent field data observations by Castagna et al. (2003) reveal similar effects at seismic frequencies, although the authors speculate that these effects can be caused by processing.

In this paper, we attempt to explain the phenomenon of frequency-dependent reflectivity of a porous fluid-saturated layer by a diffusion model with low, frequency-dependent quality-factor (Q) values. Experimental studies show that attenuation is strongly affected by the porous-medium properties and by fluid saturation (Hauge, 1981; Raikes and White, 1984; Bourbie et al., 1987; Sams et al., 1997; Dasgupta and Clarc, 1998; Goloshubin and Korneev, 2000). It is well accepted that Q is frequency dependent, changes dramatically with liquid saturation, and may be less than 10 in sedimentary rocks (Jones, 1986; Sams et al., 1997). The presence of fluids may lower Q in metamorphic rocks to 14 (Pujol et al., 1998), and in limestone from 200 (dry) to 20–40 (water saturated) (Cadoret et al., 1998). In this paper, we investigate low-frequency anomalies of seismic reflections from porous layers; these anomalies were observed in physical modeling. We also analyze vertical seismic profile (VSP) data recorded at a natural-gas storage field in Indiana. This VSP survey was a time-lapse study during which the reservoir changed from being predominantly gas saturated to being predominantly water saturated. We summarize the experiment and the conventional analysis used in Daley et al. (2000) before analyzing the low-frequency anomalies.

ULTRASONIC LABORATORY STUDY

A series of laboratory ultrasonic experiments has been conducted to investigate the wavefields reflected from and transmitted through a porous layer with varying water saturation. The physical model (Figure 1a) consisted of two 3-mm-thick Plexiglas sheets separated by a 7-mm-high sealed void filled with sandstone. The sandstone was made artificially, using a natural sand and clay mixture. To prevent an increased lateral boundary flow, the sand was glued to the surfaces of contact. The thickness of the sandstone (3 mm) was equal to the

Manuscript received by the Editor May 8, 2001; revised manuscript received September 22, 2003.
*Lawrence Berkeley National Laboratory, 90-1116, 1 Cyclotron Road, Berkeley, California 94720. E-mail: vakorneev@lbl.gov; tmdaley@lbl.gov; dsilin@lbl.gov.
‡University of Houston, Houston, Texas. E-mail: g_goloshubin@yahoo.com.
© 2004 Society of Exploration Geophysicists. All rights reserved.

thickness of the Plexiglas sheets and was much less than a dominant wavelength. Therefore, we used 2D physical modeling, where the Plexiglas was simulating a homogeneous constant-velocity background medium. The porous-layer case was hermetically sealed to allow its saturation by fluid. The grain sizes of sand and clay used in all experiments were the same. To avoid gravitational effects on fluid distribution within the porous layer, the whole physical model was placed on a horizontal table surface that was covered by a sound-insulating cloth. The velocity and density measurements of the materials are shown in Table 1. The acoustic impedance of water-saturated sandstone is higher than that for the nonsaturated sandstone. The Plexiglas has the lowest impedance. The sandstone was not vacuumed, and therefore some (as much as 10%) residual moisture was present in the "dry" medium. Correspondingly, a small amount of air was trapped in the material, when most of the pore space was saturated with water. This created more realistic partially saturated rocks, closer to field conditions, although neither of the two ideal limits seems possible.

Table 1. Velocity and density measurements for the various materials.

Material	V_p (m/s)	Density (kg/m^3)
Plexiglas	2300	1200
Dry sandstone	1700	1800
Saturated sandstone	2100	2100

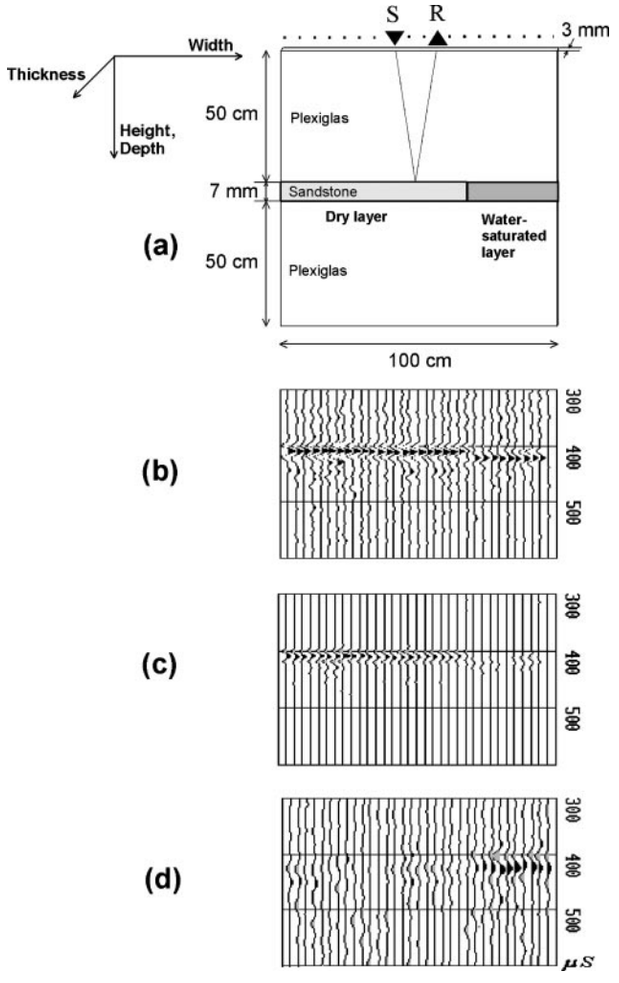

Figure 1. (a) The model and laboratory-experiment data for a 7-mm-high layer. (b) A common offset gather; (c) the same data with high-pass (60 kHz) filtering; and (d) low-pass (15-kHz) filtering. Note the strong low-frequency reflection for the water-saturated layer.

A first set of experiments used seismic-reflection acquisition geometry (Goloshubin et al., 1996), where waves reflected from the layer were recorded. The layer was 7 mm in height (h) and had 32% porosity and 300 md permeability. Data shown on Figure 1 present one example from a series of experiments. There is a significant difference between the seismic response of the porous water-saturated zone and that of the nonsaturated (dry) zone (Figure 1b). The water-saturated zone causes noticeable phase delay and loss of high-frequency energy. The recorded VSP zero-offset traces for the same model are shown on Figure 2. There is a substantial difference between the upgoing wavefield from the water-saturated layer and the upgoing wavefield from the dry layer, whereas the transmitted field shows no such difference. This common property caused by a high transmission/reflection ratio is more pronounced at low frequencies.

To measure the quality factor Q of the porous layer as a function of frequency, a set of special experiments was conducted for a thick, porous layer, whereby reflected and transmitted waves could be detected without interference between target waves and multiples. This was done for both dry and water-saturated rocks using the same VSP observation system as that shown on Figure 2. The porous layer was prepared with the same composition of sand and clay that was used for the previous experiment, and was 40 mm in height (h). We used transmitted and incident waves to determine Q in both cases, using the zero-order ray-approximation expression for the transmitted wave,

$$U = \frac{U_0 L_0}{L} T^2 e^{-\alpha h}, \tag{1}$$

where U and U_0 are recorded spectral amplitudes, L and L_0 are geometrical spreading factors for the transmitted and incident waves, and T is the computed transmission coefficient. The attenuation coefficient α was estimated from equation (1) to give

$$\alpha = -\frac{1}{h} \ln\left(\frac{UL}{U_0 L_0 T^2}\right), \tag{2}$$

where L was computed. The quality factor Q can be evaluated using the equation

$$Q = k/2\alpha, \tag{3}$$

containing wavenumber $k = \omega/V$, where ω is angular frequency. Because it was difficult to evaluate the frequency-dependent phase velocity V, instead of using equation (3), we evaluated the *apparent* quality factor Q_a:

$$Q_a = \omega/2v\alpha, \tag{4}$$

where measured propagation velocity v was taken from Table 1. The apparent quality factor Q_a is equal to quality factor Q when there is no dispersion. The measured values of Q_a, along with their theoretical approximations (obtained in the

next section), are shown on Figure 3, where the dry layer exhibits less attenuation. The surprising result consists of very low (<5) values of Q_a as well as a distinctive decrease in Q_a as frequency approaches zero.

THEORY

Consideration of reflection properties of an elastic layer, which is placed between two elastic half-spaces with the same material properties, is especially simple for normal incidence of a plane wave. In this case, a total reflection signal consists of an infinite series of multiples with decaying amplitudes. In the frequency domain, a reflection coefficient from a layer with a thickness h can be given by the expression

$$R = \frac{1-d}{1+d}\left(1 - \frac{2d}{1+d}\frac{\exp(i2hk_2)}{1-d\exp(i2hk_2)}\right); \quad d = \frac{k_2 v_2^2 \rho_2}{k_1 v_1^2 \rho_1}, \tag{5}$$

where the subscript $n = 1, 2$ of the wavenumbers $k_n = \omega/v_n$, velocities v_n, and densities ρ_n correspond to the layer and half-spaces, respectively. Parameter d in equation (5) is the elastic impedance ratio. If the duration of the incident seismic signal is less than the time interval $t_0 = 2h/v_1$ between multiples, then all the multiples are resolved and can be recorded separately. With increasing signal length, all multiples interfere, and the resulting signal becomes frequency dependent. Such frequency dependence is known as the tuning effect. At low frequencies, when $hk_2 \to 0$, all multiples cancel each other, the reflection coefficient R approaches zero, and the layer becomes invisible for seismic waves. The cancellation occurs because of the different sign of reflections from the top and bottom of the layer. If the half-spaces have different elastic properties, the respective reflection coefficients at low frequencies approach a constant value corresponding to reflection from two contacting half-spaces. Frequency dependence of R does not explain the model

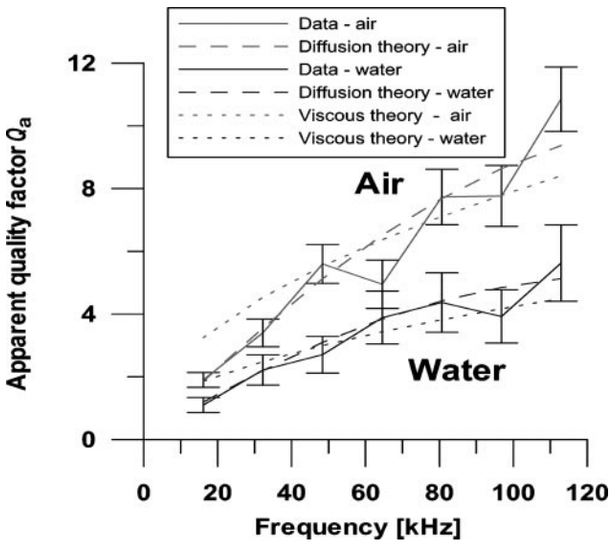

Figure 3. Apparent quality factor Q_a versus frequency, for air-saturated (red color) and water-saturated (blue color) cases. Experimental values obtained for a 40-mm layer (solid lines) are compared with a theoretical diffusive-viscous model (dashed lines) and a purely viscous model (dotted lines).

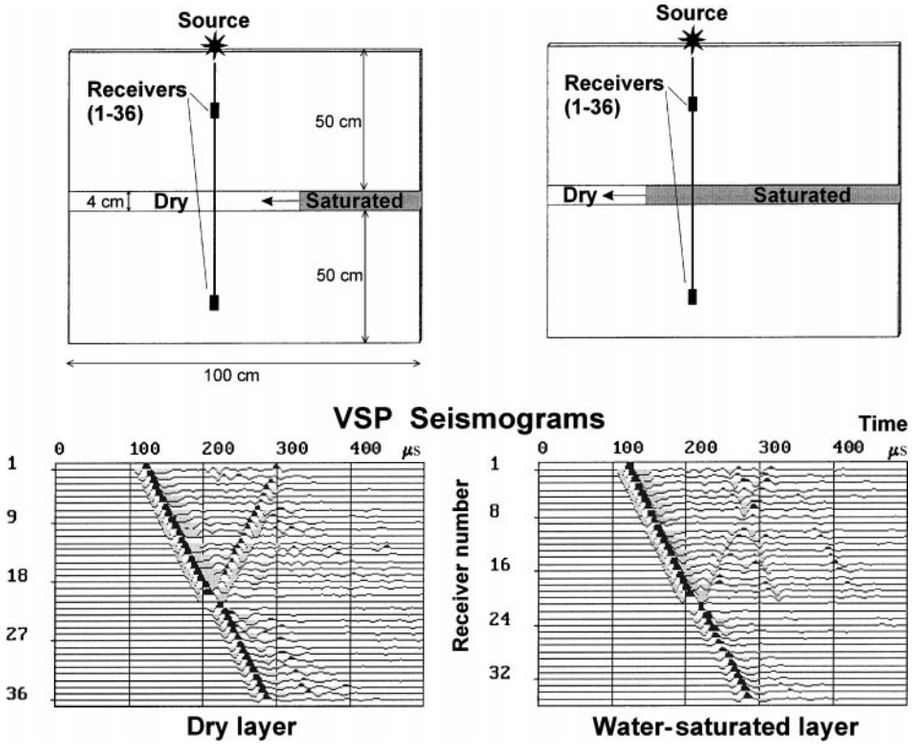

Figure 2. Physical modeling experimental setup (upper panels) and recorded traces (lower panels) for porous-layer attenuation measurements in dry (left) and water-saturated (right) layers.

data that show low-frequency reflections for a water-saturated layer producing a higher reflection amplitude than the same reflections produce for a dry layer. In the squirt flow and patchy saturation models (Mavko et al., 1998) in the low-frequency limit, Q is inversely proportional to the frequency, and therefore also cannot be used for this case.

To explain the results, we consider a scalar wave-propagation equation in the form

$$\frac{\partial^2 u}{\partial t^2} + \chi \frac{\partial u}{\partial t} - \gamma \frac{\partial^2}{\partial x^2}\frac{\partial u}{\partial t} - v^2 \frac{\partial^2 u}{\partial x^2} = 0, \tag{6}$$

where u is the displacement. The second term in equation (6) characterizes a diffusional dissipative force, whereas the third term describes viscous damping (Landau and Lifschitz, 1959). We call the coefficients χ and γ the diffusive and viscous attenuation parameters, respectively, bearing in mind that the true physical attenuation mechanisms are still unclear. Parameter v is the constant wave-propagation velocity in a nondissipative medium. We seek a solution in the form of a harmonic wave

$$u = \exp(i\tilde{k}x)\exp(-i\omega t); \quad \tilde{k} = k + i\alpha, \tag{7}$$

with the wave number k, attenuation coefficient α, and angular frequency ω. By substituting equation (7) in equation (6) and employing some algebra, we obtain the expressions

$$k = k_0 \sqrt{\frac{\sqrt{(1+dg)^2 + (d+g)^2} + 1 + dg}{2(1+g^2)}}, \tag{8}$$

$$\alpha = k_0 \sqrt{\frac{\sqrt{(1+dg)^2 + (d+g)^2} - 1 - dg}{2(1+g^2)}}, \tag{9}$$

with $k_0 = \omega/v$, and dimensionless parameters

$$d = \frac{\chi}{\omega}; \quad g = \frac{\omega\gamma}{v^2}. \tag{10}$$

Dependencies of normalized phase velocity $V_p/v = \omega/kv$ and attenuation factors on normalized frequency are shown on Figure 4 for two interesting cases, $\gamma = 0$ and $\chi = 0$.

When $\gamma = 0$, we have asymptotic evaluations

$$Q = \frac{1}{2}, \text{ and } Q_a = \frac{1}{2\sqrt{d}} = \frac{1}{2}\sqrt{\frac{\omega}{\chi}} \tag{11}$$

for low frequencies ($d > 1$), and

$$Q = Q_a = \frac{1}{2d} = \frac{\omega}{2\chi} \tag{12}$$

for high frequencies ($d < 1$).

In the second case, when $\chi = 0$,

$$Q = Q_a = \frac{1}{g} = \frac{v^2}{\gamma\omega} \tag{13}$$

for low frequencies ($g < 1$), and

$$Q = \frac{1}{2}, \text{ and } Q_a = \sqrt{\frac{g}{2}} = \sqrt{\frac{\gamma\omega}{2v^2}} \tag{14}$$

when $g > 1$. The apparent quality factor Q_a reaches a minimum value of $\sqrt{2}$ at $g = \sqrt{3}$.

Using asymptotic expressions for the attenuation coefficient and the wavenumber, we infer that at low frequencies, the first inertial-force component in the wave equation (6) can be neglected and the latter becomes parabolic

$$\chi \frac{\partial u}{\partial t} - \gamma \frac{\partial^2}{\partial x^2}\frac{\partial u}{\partial t} - v^2 \frac{\partial^2 u}{\partial x^2} = 0. \tag{15}$$

After substitution of form (7) into equation (15), we obtain

$$\alpha = \sqrt{s\left(\omega\gamma + \sqrt{\omega^2\gamma^2 + v^4}\right)};$$
$$k = \sqrt{s\left(-\omega\gamma + \sqrt{\omega^2\gamma^2 + v^4}\right)}, \tag{16}$$

where $s = \chi\omega/2v^4$.

We applied the obtained results to ultrasonic Q_a measurements for the 40-mm-thick layer presented in Figure 3 to obtain estimations of the attenuation parameters. Accordingly, the values of attenuation parameters (diffusion-viscous

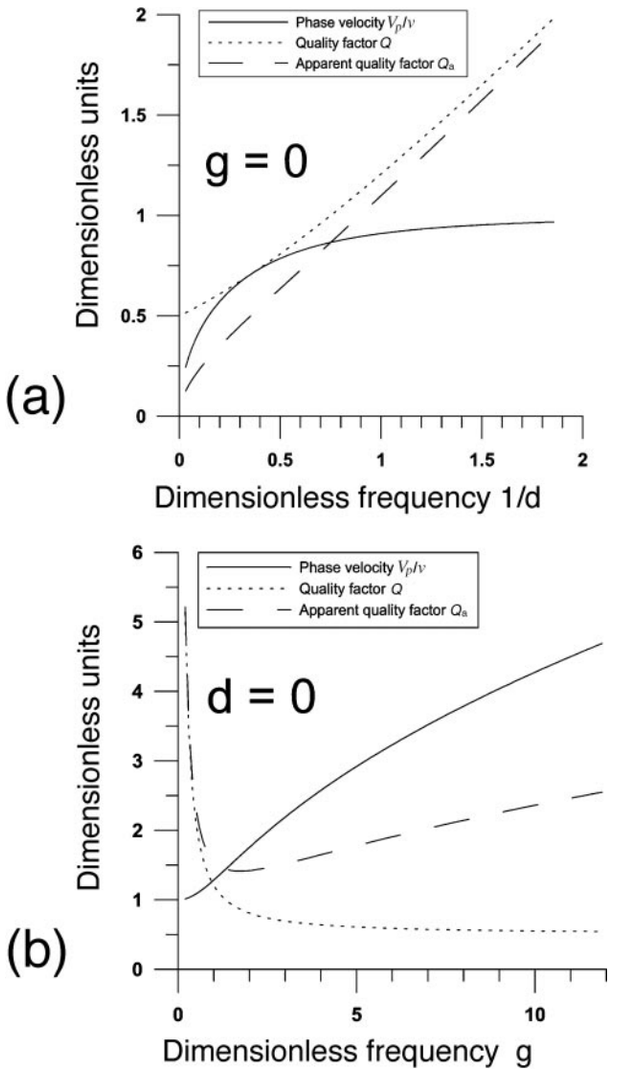

Figure 4. Normalized phase velocity $V_p/v = \omega/kv$ (solid line), attenuation factor Q (dotted line), and apparent attenuation factor Q_a (dashed line) as functions of nondimensional frequency for (a) $\gamma = 0$ and (b) $\chi = 0$ cases. All three quantities are dimensionless and plotted on the same vertical axis.

model) in the porous layer were estimated to be $\chi = 56$ kHz, $\gamma = 0.056$ m^2/s for the dry layer, and $\chi = 90$ kHz, $\gamma = 0.2$ m^2/s for the water-saturated layer. The theoretical curves are shown on Figure 3, together with the physical model experimental data. As it follows from Figure 3, the increase of Q_a with frequency can also be a result of high frequency dependence of the purely viscous attenuation model (when $\chi = 0$), if the recording frequency is above the Q_a minimal value. The viscous-theory curves in Figure 3 were found using the values $\gamma = 120$ m^2/s for dry cases and $\gamma = 280$ m^2/s for water-saturated cases.

These two sets of estimates for attenuation parameters were used for comparison of reflected waves in theoretical and experimental data from Figure 1 obtained for the 7-mm layer. The reflection-coefficient ratios (water-saturated/dry in Figure 5) were computed using equation (5), where k_2 was a complex value. Note that in this case, the impedance ratio d from equation (5) depends on frequency and estimated attenuation parameters χ and γ. The purely viscous model gave an increase of the amplitude ratio with frequency and no resonant peaks. It also gave a much smaller than observed time delay (Figure 6). To match the position of peaks for the mixed diffusion-viscous set, we reduced velocities by a factor of 0.7 in the layer, so that they had values $V_p = 1190$ km/s for the dry case and $V_p = 1470$ km/s for the water-saturated case. This change also reproduced the notch on the traveltime delay curve. After this correction, our theoretical formulation with a diffusive-viscous loss mechanism matches the physical model data reasonably well. The justification of this correction will be described in the discussion section. The theoretical values of Q_a factors on Figure 3 were computed using the corrected layer velocities. In Figure 5, we also show theoretical results for waves reflected from a half-space with the elastic parameters of the porous medium.

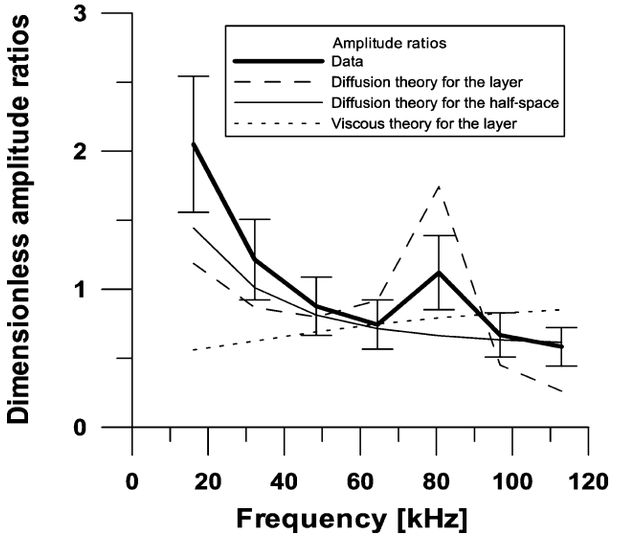

Figure 5. Reflection-coefficient ratios (water-saturated/dry) versus frequency computed from data (thick solid line), theoretical diffusive-viscous model (dashed line), and purely viscous model (dotted line). The estimates for parameters γ and χ were obtained after fitting measured Q_a values (see Figure 3). A theoretical curve for a diffusive-viscous half-space is shown as thin solid line.

Field experiment: VSP monitoring

To test the field-scale applicability of frequency-dependence analysis based on the diffusive-attenuation theory shown above, we analyzed VSP data recorded at a natural-gas storage field in Indiana. This VSP survey was a time-lapse study during which the reservoir changed from being predominantly gas saturated to being predominantly water saturated. We summarize the experiment and the conventional data analysis, as were used in Daley et al. (2000), before demonstrating the low-frequency effects.

Background

The Northern Indiana Public Service Company (NIPSCO) operates naturally fractured reservoirs for seasonal storage of natural gas. The reservoir is in NIPSCO's Royal Center field in northern Indiana. The gas is injected during summer and withdrawn for consumer use during winter. As part of DOE-sponsored research in fractured gas production, Lawrence Berkeley National Laboratory (LBNL) conducted a VSP experiment to aid a delineation of NIPSCO's reservoir and to study the seismic effects of variable gas saturation. The annual displacement of water by gas within the natural fractures of the reservoir made this field a good candidate for time-lapse monitoring.

The reservoir we studied, the Trenton Formation, is a Paleozoic Ordovician dolomite that is part of the mostly shale and carbonate stratigraphy of the Royal Center field. The Trenton Formation is overlain by Pleistocene gravel, Silurian-age limestone and shale, Ordovician-age limestone, and (immediately above the Trenton) a 76-m-thick section of the Ordovician Eden Group shale. The field operators believe that the top section of the Trenton Dolomite is unfractured and forms a cap for the reservoir. The thickness of the fractured reservoir

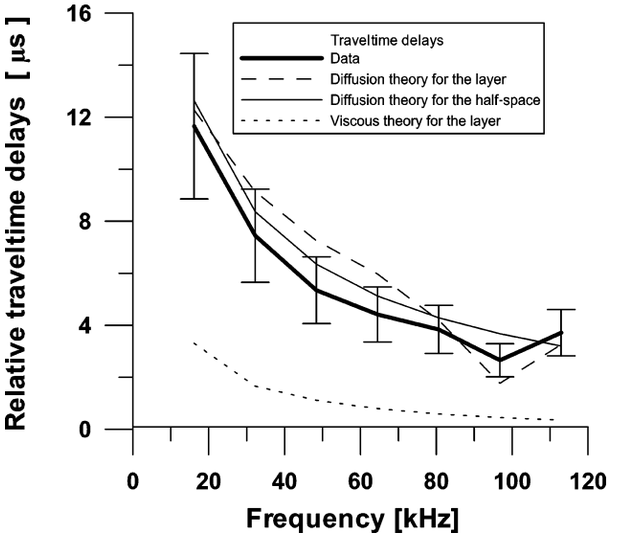

Figure 6. Traveltime delays of a reflected wave from a dry layer with respect to a water-saturated layer. Data curve (thick solid line) is compared with the theoretical diffusive-viscous model (dashed line) and purely viscous model (dotted line). A theoretical curve for a diffusive-viscous half-space is shown as thin solid line.

is approximately 9 m. There were two phases of time-lapse VSP acquisition at the field site, with essentially identical acquisition geometry (i.e., source and receiver locations) under distinctly different reservoir conditions. During the initial survey in December 1996, the reservoir gas pressure was near its maximum of about 400 psi; during the second survey in May 1997, the reservoir gas pressure was reduced to about 250 psi. Because the natural water pressure within the Trenton Formation is about 310 psi, the reservoir was mostly gas saturated in the 1996 survey and mostly water saturated in the 1997 survey.

Acquisition

There were four, nine-component VSP data sets acquired, plus a walkaway VSP. The sensors were three-component, wall-locking geophones (with a 14-Hz corner frequency) in a five-level string with 2.4-m spacing between sensor depths. The vibroseis sources (both P- and S-wave) used a 12- to 99-Hz sweep, 12 s long and with a 3-s listen time recorded at a 1-ms sample rate. The S-wave trucks were positioned at each source site such that they generated an inline (S1) and a crossline (S2) polarized shear wave, relative to the line connecting the source location and the well. A schematic of the source locations and offsets is shown in Figure 7. Field conditions restricted the available source locations to those shown. Our analysis in this paper will focus on site 1, the 30-m source-offset VSP, which had sensor depths from 90 to 332 m at 2.4-m intervals. The site 1 data will hereafter be referred to as the zero-offset VSP. Also presented here are results from the walkaway survey, which had sensor depths from 300 to 310 m at 2.4-m intervals, and source locations from 61 to 472 m at 15-m intervals. The May 1997 survey successfully repeated the December 1996 survey.

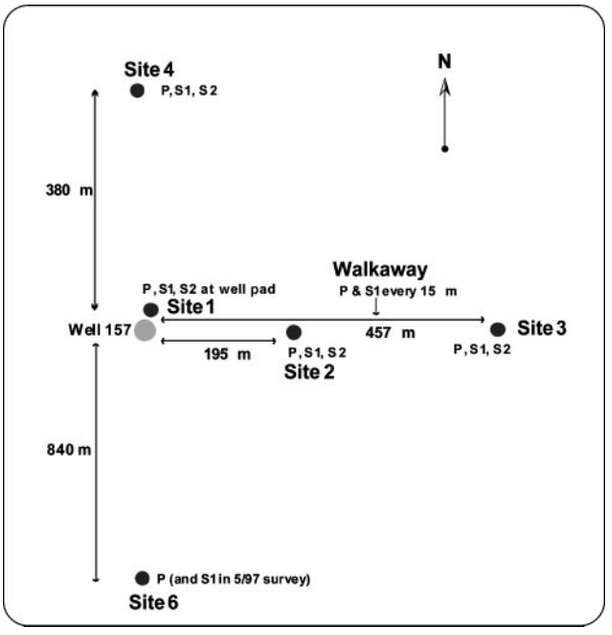

Figure 7. Source locations for the NIPSCO time-lapse VSP experiment. All source locations were repeated, except the site-6 S-wave. Only site-1 and walkaway data are discussed in this paper.

Processing

The VSP data processing was performed primarily using conventional seismic processing packages. The frequency-dependence analysis was done using LBNL software. The processing flow for each data set was as follows. (1) Convert data from field-formatted data tapes. (2) Edit and stack uncorrelated traces. Both manual and automated editing was required because of background noise. (3) Correlate traces, and sort by source type. (4) Use P-wave arrival to calculate horizontal-component geophone rotation angles. (5) Use the calculated rotation angles to rotate each source-type data set into vertical, horizontal inline and horizontal crossline geophone orientations. (6) Pick arrival times, calculate P- and S-wave velocities and Poisson's ratio. (7) For zero offset, use S-wave arrivals to measure S-wave splitting. (8) Use F-K filters to separate downgoing and upgoing wavefields.

Zero-offset VSP analysis

The two time-lapse data sets were analyzed initially for temporal variations in P- and S-wave traveltime, as well as for other attributes (Daley et al., 2000). Figure 8 shows the time-lapse P-wave traveltime change, and Figure 9 shows the time-lapse S-wave traveltime change. Traveltime picking was tested using cross correlation of first-arrival wavelets and hand picking of peaks or zero crossings, with results in agreement for all methods (including interpolation for subsample accuracy). When we compared the measured traveltimes for 1996 and 1997, we found no change in P-wave or S-wave time that was attributable to the reservoir (within the scatter of the data points

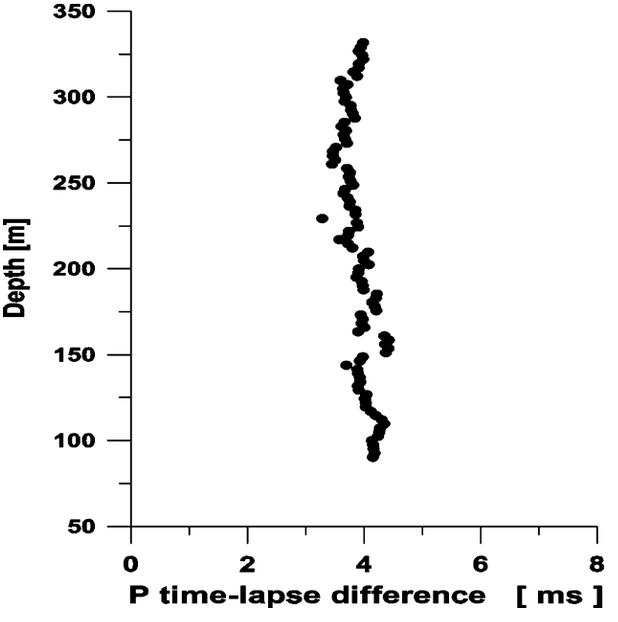

Figure 8. Time-lapse change for the NIPSCO VSP P-wave data from site 1 (a 30-m offset). We show the difference in P-wave arrival time, at each recorded depth, between the 1996 (gas-saturated reservoir) and 1997 (water-saturated reservoir) data. No change was observed in the reservoir horizon (~300–310 m) compared with the other horizons, within the scatter in the data.

and allowing for a static time shift that is attributable to near-surface conditions).

No clear evidence of time-lapse changes in S-wave splitting or other anisotropic wave-propagation properties could be attributed to the reservoir horizon. High velocity in the reservoir (about 5500 m/s for P-waves), which led to long wavelengths (about 100 m), and a relatively thin fractured interval (about 9 m), are believed to have limited the detectability of fracture-induced anisotropy. The larger-offset source sites did have some time-lapse traveltime changes. However, ray-trace modeling performed using the VSP interval velocities showed that very little propagation was within the reservoir for the offset VSP sites. Because of the raypath limitations, the larger-offset VSP data could not spatially constrain the observed time-lapse changes to be within the reservoir horizon. Therefore, VSP traveltime measurements, both zero offset and larger offset, were not interpreted by Daley et al. (2000) as being affected by changes in reservoir gas saturation. However, this conventional traveltime analysis of the zero-offset VSP data did not account for frequency-dependent effects; these effects will be described below. Of the data analyzed using conventional traveltime analysis, only the P-wave walkaway was interpreted as having a small time-lapse change within the reservoir horizon. The walkaway analysis is described next.

Walkaway VSP analysis

A walkaway VSP is a survey in which the sensors are fixed and data from multiple source locations (usually along one azimuth) are recorded. The NIPSCO P-wave walkaway data were analyzed by comparing the time-lapse changes at the shallowest sensor (300 m) with the changes at the deepest sensor (310 m). Without knowing the actual reservoir interval (production is over a large perforated-casing interval), these sensors straddle the "best guess" of the reservoir available from field engineers (984 to 1016 f [300 to 310 m]). We hypothesize that the deeper sensor will record a larger time-lapse traveltime change (because of velocity changes within the reservoir that were induced by changing from predominantly gas saturation to water saturation). Figure 10 shows a consistent 0.1- to 0.5-ms difference in the time-lapse delay between the two walkaway sensor depths. Whereas the zero-offset data (Figures 8 and 9) had equivalent-magnitude traveltime changes (0.5 to 1 ms), there was a much larger standard deviation in the data. In the walkaway VSP data, the mean traveltime change for the 27 walkaway source locations is 0.2 ms, with a standard deviation of 0.1 ms. The consistency of the time-lapse difference gives us confidence that this observation is caused by physical property changes within the reservoir zone. However, the relatively small change in traveltime (less than one digital-sample interval) caused us to pursue other analytic techniques to confirm the observation of time-lapse changes. Frequency-dependence analysis based on diffusion attenuation theory provides another analytic technique.

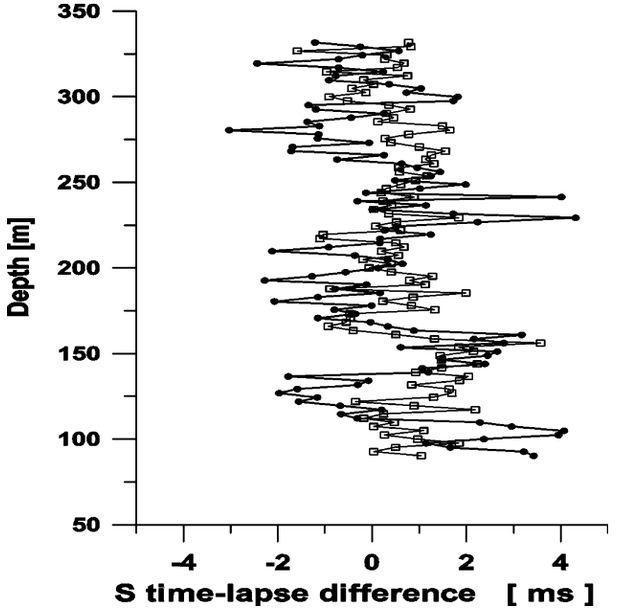

Figure 9. Time-lapse change for the NIPSCO VSP S-wave data from site 1 (a 30-m offset). We show the difference in S-wave arrival time, at each recorded depth, between the 1996 (gas-saturated reservoir) and 1997 (water-saturated reservoir) data, for two east-west (circles) and north-south (squares) polarizations of shear wave. No change was observed in the reservoir horizon (~300–310 m) compared with the other horizons, within the scatter in the data.

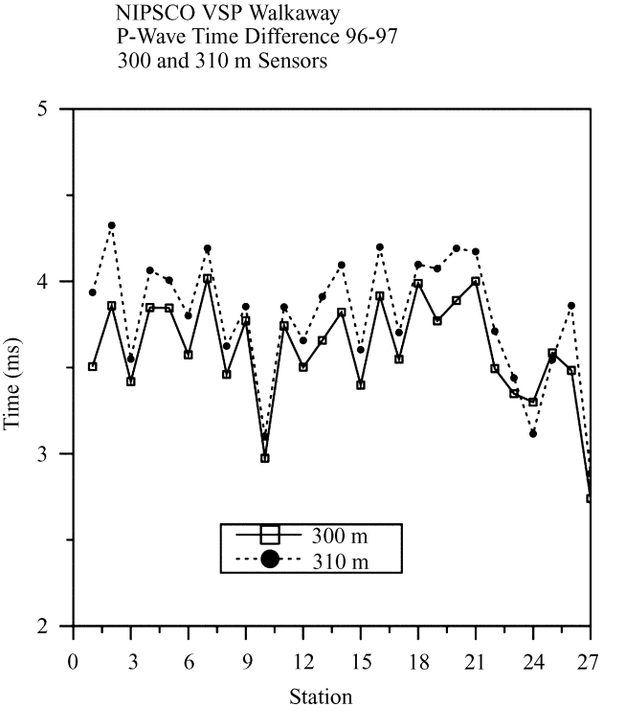

Figure 10. Time-lapse traveltime change for the NIPSCO VSP P-wave walkaway data, computed for the two walkaway sensor depths that straddle the estimated reservoir interval, for 27 source stations (from 30- to 459-m offsets at 15-m intervals). Each data point is the difference between the traveltime measured in 1996 (gas-saturated reservoir) and 1997 (water-saturated reservoir). A slight increase in traveltime change is observed at the deeper sensor (310 m) relative to the shallower sensor (300 m). This minimal change, averaging 0.2 ms, is the conventional (non-frequency-dependent) processing result, which we interpret as resulting from the change in reservoir properties.

Frequency-dependence analysis of field VSP data

Traces from Figures 11 and 12 show the downgoing wavefield and illustrate the good repeat of data collection during the surveys of December 1996 and May 1997. There are practically no differences between the 1996 and 1997 downgoing wavefields (as indicated by the conventional analysis). There are some differences between 1996 and 1997 upgoing wavefields (Figure 13). In particular, the reservoir zone reflection wave train has changes (Figure 14). To understand these changes, we have applied frequency-dependent processing to the VSP data recorded in the interval from 207 to 283 m for the 1996 and 1997 surveys. The processing included time alignment and amplitude correction of the upgoing traces, using reflections above the target horizon. Then we windowed the records on each trace, by use of a 60-ms tapering window leaving the target reflected phase. We computed the average values for amplitude-spectra ratios (where 1997 data were related to 1996 data). Amplitude ratios and traveltime delays were computed from spectral amplitude and phase. Spectral-amplitude ratios and traveltime delays for the reservoir reflection are shown using solid lines on Figures 15 and 16, respectively. The traveltime delay was computed by subtracting the two phase angles and dividing by frequency, at each frequency sampled. By using temporal ratios, we are removing the frequency-dependent sensor response and source function. Frequency-dependent

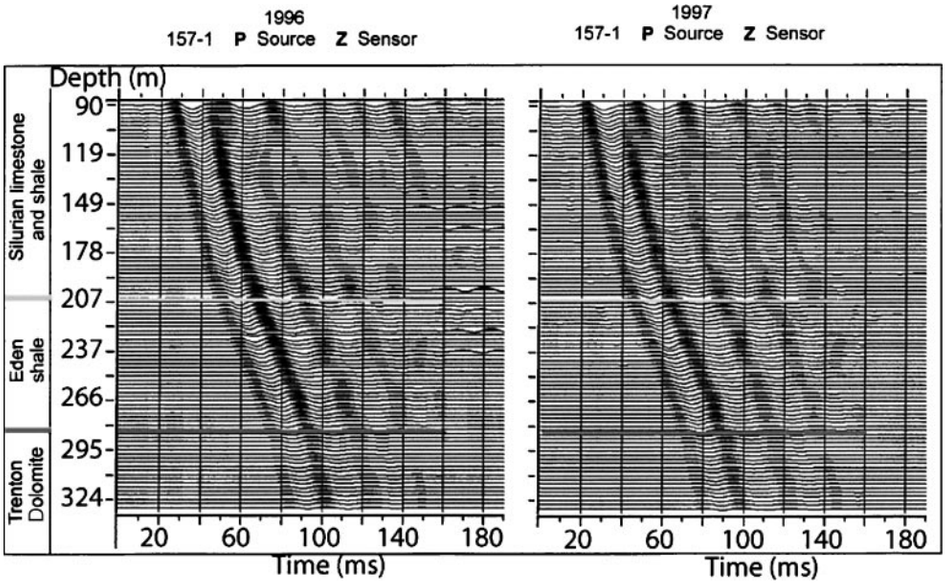

Figure 11. Downgoing wavefields for 1996 (left) and 1997 (right) show no visible changes, except a constant time shift associated with near-surface effects.

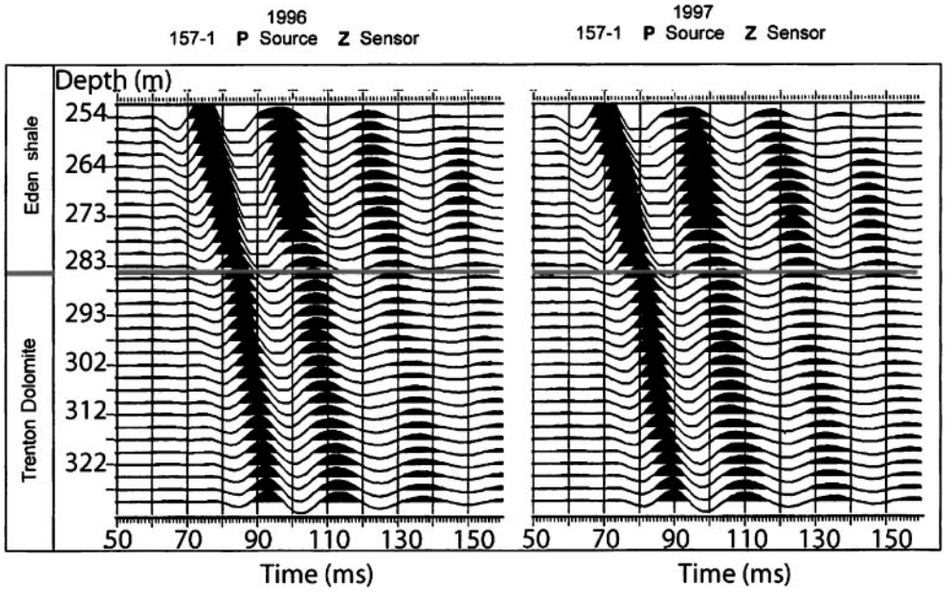

Figure 12. Zoom of traces from Figure 11, for the 254- to 329-m depth interval.

artifacts from acquisition equipment can be significant near the sensor's corner frequency and near the low-frequency part of the vibroseis sweep. Because the same source and sensors were used in both surveys, their effects should be canceled by using a ratio. Frequency-dependent effects that result from coupling the source and sensor to the earth are also minimized.

For comparison purposes, we have computed the same functions for a time window centered on the event which arrives 100 ms later and corresponds to a reflection from below the target horizon (shown on Figures 15 and 16, using dashed lines). This reflection event has been transmitted through the reservoir rather than reflected from the top of the reservoir.

In Figures 15 and 16, we can quantify the frequency-dependent effects of the change from gas-filled reservoir (1996) to water-filled reservoir (1997) and compare the reservoir reflection to a deeper reflection. Figure 15 shows a clear frequency-dependent amplitude response. The reservoir reflection (solid line) increases in amplitude from 0.6 to 1.5 as frequency decreases to 15 Hz. Figure 16 shows the frequency-dependent traveltime delay, with delay increasing from near

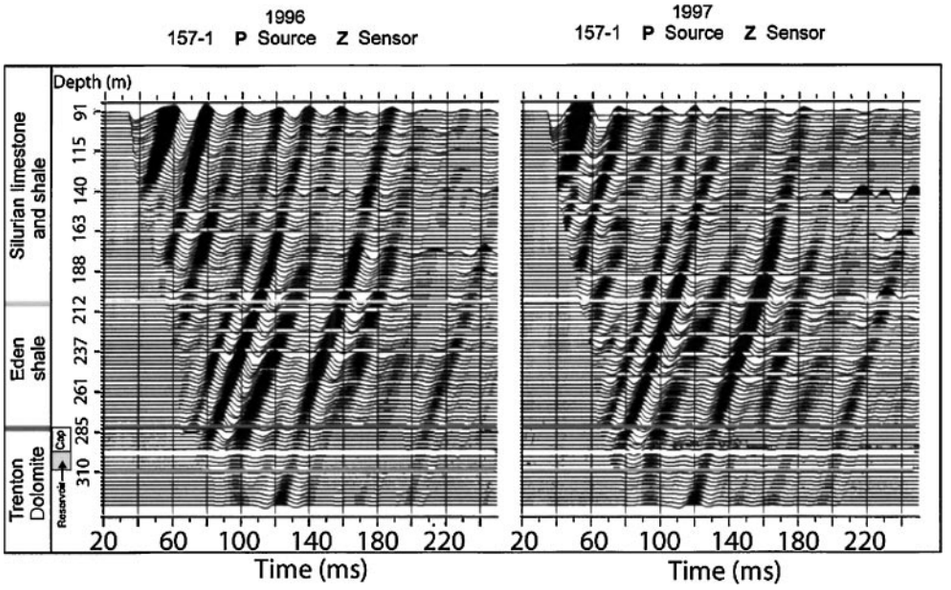

Figure 13. Upgoing wavefields for 1996 (left) and 1997 (right) reveal low-frequency changes for reflections from the Trenton Dolomite.

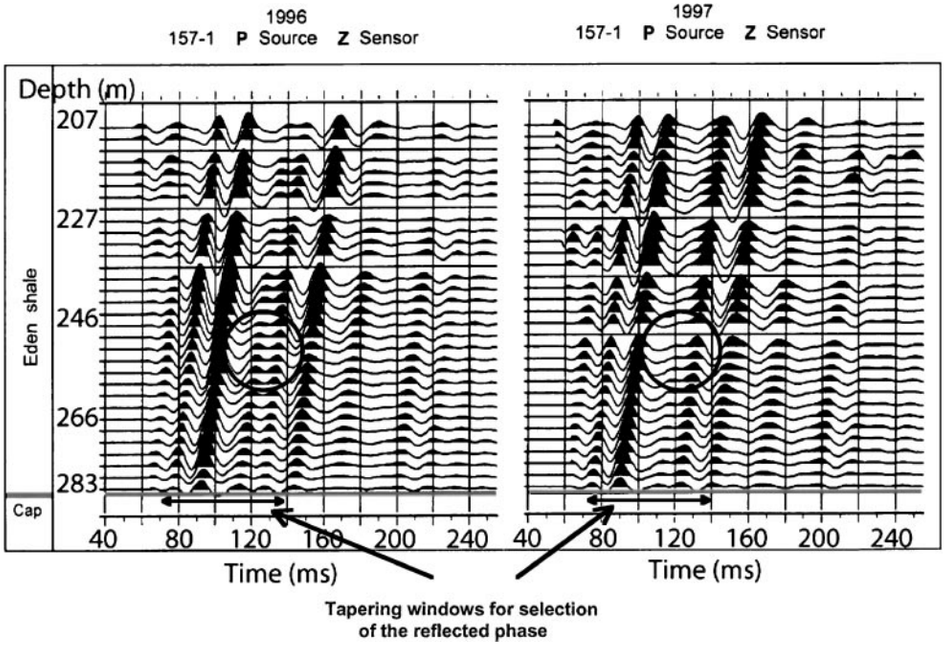

Figure 14. Zoom of traces from Figure 13, above the reservoir, which were used in frequency-dependence analysis.

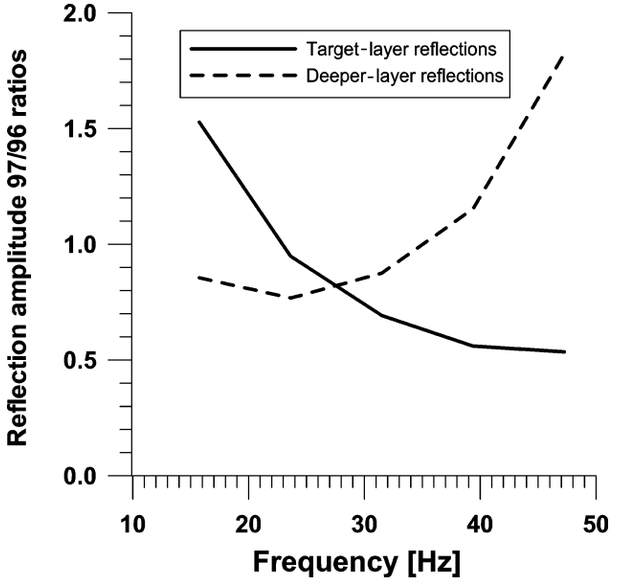

Figure 15. Spectral amplitude ratios of water-saturated (1997) to gas-saturated (1996) data. The curves were computed using amplitude spectra of reflected phases. Reflections from the reservoir (solid line) and the reflections from a deeper horizon (dashed line) show opposite characters of frequency dependence. The increase in amplitude ratio observed at low frequencies in these field data agrees with theoretical predictions for a diffusive-viscous model (Figure 5).

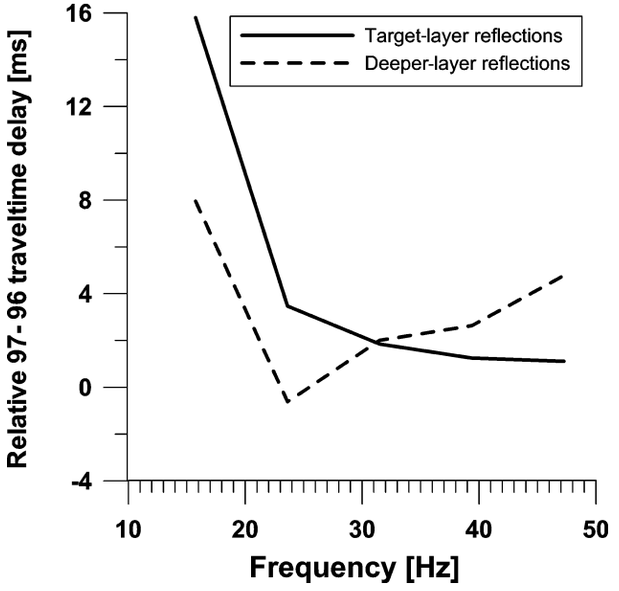

Figure 16. Traveltime delays of water-saturated case (1997) data compared with the gas-saturated (1996) case data. The curves are computed from the argument of the complex spectral ratios. Delays for reservoir reflection (solid line) are more pronounced than are the delays for a later-arriving phase (dashed line). The increasing delay observed at low frequencies in these field data agrees with theoretical predictions for a diffusive-viscous model (Figure 6).

zero to 15 ms as frequency decreases to 15 Hz for the reservoir reflection.

DISCUSSION

The observed and computed data covered a wide frequency band, $0.1 \leq h/\lambda \leq 1.0$, where λ is a wavelength within the layer. Laboratory measurements revealed increased reflectivity and apparent phase delay at the low-frequency end of the spectra. A purely elastic theoretical model could not explain these results, which gave a higher reflectivity for the dry case. Laboratory measurements of Q_a for a porous layer revealed very low values for both dry- and water-saturated cases and a steady Q_a decrease as frequency approached zero. Such behavior of Q_a was modeled by incorporating a diffusive attenuation-dissipation term with attenuation parameter χ into the equation of motion (6). The estimated values of χ allowed us to correctly describe the observed amplitude and phase-frequency dependencies, which are most profound when $\omega < \chi$. The increased saturation gave a larger value of χ compared with the mostly gas-saturated case. Consideration of other mechanisms included the tuning effect, which in particular is responsible for resonance peaks on Figure 5. Whereas in the purely elastic case all multiple reflections tend to cancel each other out at low frequencies, the diffusion-attenuation mechanism changes the cancellation balance, and observation of reflections from very thin layers becomes possible.

To match the physical-model data, we had to reduce velocities inside of the porous layer by a factor of 0.7. The velocities shown on Table 1 were measured in a special experiment using first-arriving phases. Poroelastic theory predicts the existence of the slow waves in fluid-bearing rocks (Biot, 1956). These waves can have very high attenuation and rarely can be recorded, but they certainly contribute in the reflection-transmission processes at interfaces between layers. In the described theoretical model, we use a single effective-phase velocity, which is likely to have values lower than the fastest measured velocity. In our case, the effective-phase velocity is 70% of the measured first-arrival velocity. In the water-saturated case, the reduced value of velocity $V_p = 1470$ km/s in the layer is very close to the propagation velocity in the water, which suggests that pore-fluid properties make the major contribution in the effective-velocity value. The theoretical and measured curves from Figures 3 and 5 match quite well for both phases and amplitudes, whereas the coefficients χ and γ used in these calculations were estimated from the 40-mm-high layer of Figure 3. This indicates that the proposed theory and the data are consistent.

In the field example presented of gas-reservoir monitoring, standard VSP data processing did not reveal any significant changes between a gas- and a water-saturated reservoir, whereas the changes in reflectivity are substantial at low frequencies. The observed increase in amplitude and traveltime delay as frequency decreases is in agreement with theoretical predictions and laboratory results. The spectral ratio for a later arrival, which was transmitted through the reservoir, increases with frequency, which is also consistent with the predicted opposite character of frequency dependence for reflected and transmitted energy.

The similarity between field VSP data results and laboratory data results is striking. Both amplitude ratios as well as

traveltime delays have the same character of frequency dependence, which suggests that a similar intrinsic mechanism is responsible for the low-frequency effect. On the other hand, the low values of Q_a in our ultrasonic experiment do not allow simple extrapolation of Q_a versus frequency dependencies into the seismic frequency range. This means that the dependence of attenuation parameters χ and γ on porosity, permeability, stiffness, and other liquid-saturated rock parameters may be different for different frequency ranges. Another explanation may be in the intrinsic structure of fluid-bearing rock. While in the laboratory study the pore sizes were of the order of 10^{-4} m, scaling gives an order of 10^{-1} m for the fluid containing element in the field experiment. It is consistent with the fact that NIPSCO's reservoir was a fractured dolomite, which has very low matrix porosity, and therefore water and gas were stored in fractures. In both the laboratory and field data, the observed effects can be attributed to the target-reservoir horizon and are not present on other parts of the seismic record. These findings are especially important, because no significant changes were found in the full frequency content seismic reflections from the field reservoir.

The definition of low frequency range mostly depends on the value of attenuation parameter χ. Whereas the thickness of a layer must be less than a fraction of a wavelength to make sure that all strong multiples are in phase, the layer-attenuation parameter χ should be on the order of the frequency used to ensure profoundness of the found amplitude and phase effects.

Physical interpretation of the diffusion-dissipation term remains uncertain. We speculate that fluid flow in the matrix can be the main driving mechanism of this effect. The fluid flow must be especially important at low frequencies, whereas at high frequencies it might not occur at all.

CONCLUSIONS

Both laboratory and field studies of gas- and fluid-saturated porous reservoirs revealed noticeable changes in seismic reflections at low frequencies. Reflection coefficients decrease when frequency increases. Seismic reflections also have traveltime delays, which become more profound as frequency approaches zero. These effects are greater in porous media that are mainly water saturated, compared with the effects in mainly gas saturated media. The effects can be explained by adding a diffusional term into the wave equation and take place at a very low apparent quality factor ($Q_a < 5$).

Application of low-frequency analysis allowed us to find changes in time-lapse VSP field data, which include the effects of stronger reflections and traveltime delays when gas was replaced by water. These properties can be used to detect and monitor water- and gas-saturation changes in porous layers. We speculate that fluid flow and (or) internal friction between grains are the major driving mechanisms of the found phenomena.

ACKNOWLEDGMENTS

This work was supported by the Office of Science, Office of Basic Energy Sciences, Division of Engineering and Geosciences of the U.S. Department of Energy under Contract No. DE-AC03-76SF00098. The modeling results were provided by the Western-Siberian Research Institute for Geology and Geophysics (ZapSibNIIGG). The NIPSCO VSP was supported by the assistant Secretary for Fossil Energy, National Energy Technology Laboratory. We would like to thank four anonymous reviewers whose comments helped to substantially improve the paper.

REFERENCES

Biot, M. A., 1956, Theory of propagation of elastic waves in a fluid-saturated porous solid. I. Low-frequency range: Journal of the Acoustical Society of America, **28**, 168–178.

Bourbie, T., Coussy, O., and Zinszner, B., 1987, Acoustics of porous media: Editions Technip.

Cadoret, T., Mavko, G., and Zinszner, B., 1998, Fluid distribution effects on sonic attenuation in partially saturated limestones: Geophysics, **63**, 154–160.

Castagna, J. P., Sun, S., and R. W. Siegfried, 2003, Instantaneous spectral analysis: detection of low-frequency shadows associated with hydrocarbons: The Leading Edge, 120–127.

Daley, T. M., Feighner, M. A., and Majer, E. L., 2000, Monitoring underground gas storage in a fractured reservoir using time-lapse VSP: Lawrence Berkeley National Laboratory Report LBNL-44876.

Dasgupta, R., and Clarc, R. A., 1998, Estimation of Q from surface seismic reflection data: Geophysics, **63**, 2120–2128.

Goloshubin, G. M., and Bakulin, A. V., 1998, Seismic reflectivity of a thin porous fluid-saturated layer versus frequency: Expanded Abstracts, 68th SEG Meeting, New Orleans, 976–979.

Goloshubin, G. M., and Korneev, V. A., 2000, Seismic low frequency effects for fluid saturated porous media: 70th Annual International/ Meeting; SEG, Expanded Abstracts, 976–979.

Goloshubin, G. M., Verkhovsky, A. M., and Kaurov, V. V., 1996, Laboratory experiments of seismic monitoring: Expanded Abstracts, 58th European Association of Exploration Geophysicists Meeting, P074.

Hauge, P. S., 1981, Measurements of attenuation from vertical seismic profiles: Geophysics, **46**, 1548–1558.

Johnston, D. H., and Toksoz, M. N., 1981, Seismic wave attenuation: SEG.

Jones, T. D., 1986, Pore fluids and frequency-dependent wave propagation in rocks: Geophysics, **51**, 1939–1953.

Landau, L. D., and Lifschitz, E.M., 1959, Fluid mechanics: Pergamon Press.

Mavko, G., Mukerji, T., and J. Dvorkin, 1998, The Rock physics handbook: Tools for seismic analysis in porous media: Cambridge University Press.

Pujol, J. M., Luschen, E., and Hu, Y., 1998, Seismic wave attenuation in metamorphic rocks from VSP data recorded in Germany's continental super-deep borehole: Geophysics, **63**, 354–365.

Raikes, S. A., and White, J. E., 1984, Measurements of earth attenuation from downhole and surface seismic recording: Geophysical Prospecting, **32**, 892–919.

Sams, M. S., Neep, J. P., Worthington, M. H., and King, M. S., 1997, The measurement of velocity dispersion and frequency-dependent intrinsic attenuation in sedimentary rocks: Geophysics, **62**, 1456–1464.